

# Characterization of tin oxide nanoparticles synthesized by discharging the non-thermal plasma jet in liquid and their application as an antibacterial agent

Omar O. Abdulhadi<sup>1,\*</sup> , Hamsa A. Ali<sup>2</sup>, Ahmed S. Obaid<sup>2</sup>

<sup>1</sup>Ministry of Education, Direction of Education in AL-Anbar, Anbar, Iraq.

<sup>2</sup>College of Science, University of Anbar, Anbar, Iraq.

\*Corresponding author: [ayhamomar07@gmail.com](mailto:ayhamomar07@gmail.com)

## Original Research

## Abstract:

Received:  
20 August 2024  
Revised:  
8 November 2024  
Accepted:  
21 November 2024  
Published online:  
30 December 2024

© The Author(s) 2024

This study reports the synthesis of tin oxide nanoparticles using a non-thermal plasma jet technique. Spectroscopic analysis (OES) of plasma was carried out at atmospheric pressure to measure the plasma parameters used in the synthesis of nanoparticles. SnO<sub>2</sub> NPs were synthesized at different durations (3 and 5 minutes) using a DC-high-voltage power source with a voltage of 13 kV. X-ray diffraction (XRD) showed that SnO<sub>2</sub> NPs, prepared in 3 minutes, are rutile tetragonal polycrystalline and have an average crystallite size of 12.45 nm. Field emission scanning electron (FE-SEM) images also show that the nanoparticles are spherical and homogenous, with an average nanostructure diameter of 25 to 45 nm for both (3 and 5 minute) preparation times. UV-Vis spectroscopy showed peaks of surface plasmon resonance around 255 – 260 nm. The ICP-mass technique was used to evaluate nanoparticle concentrations, which were between 90 – 100 µg/mL. Zeta potential (ZP) measurements revealed that the particles are relatively stable colloids. The study shows that synthesized nanoparticles have exceptional antibacterial efficacy against *Escherichia coli* and *Staphylococcus aureus* bacteria. These nanoparticles are low-cost, scalable, and can be synthesized using gas or liquid phases, enabling the synthesis of a wide range of nanoparticles suitable for various pathogenic bacterial types.

**Keywords:** Tin oxide nanoparticles; Non-thermal plasma jet; Plasma diagnosis; Antibacterial agent

## 1. Introduction

The high prevalence of infectious diseases and the increasing drug resistance of pathogenic microorganisms are highly concerning. Although there has been a lot of progress in understanding microbial causes and using advanced therapy, the morbidity and death rates related to microbial infections continue to be high [1]. New antimicrobial agents are critical for controlling microbial diseases; hence, inorganic disinfectants, including metal oxide nanoparticles, are very interesting.

Over the past decade, remarkable developments have been made in synthesizing nanoparticles made from metal oxides, which are crucial in various fields of science [2]. Many techniques that have been used for synthesizing nanomaterials. The previously approved techniques have some drawbacks,

including the high cost of reactive materials and their effects on public health. The synthesis of nanomaterials for biomedical applications necessitates alternative methods that do not involve toxic chemicals. Conventional methods require toxic reducing or oxidant agents to synthesis stable nanoparticles, making alternative synthesis crucial for the development of nanotechnology. Therefore, we should develop a mechanism to overcome these challenges and advance research on colloidal nanoparticles. Non-thermal liquid plasma systems have recently seen increased interest due to their important properties in antimicrobial, sterilization, biomedical, and other future applications, including nanotechnology and environmental remediation [3]. Metal oxide nanoparticles have high inhibitory activity against many types of pathogenic bacteria, and their activity in inhibiting bacteria is influenced by factors, the most

important of which are particle size, type of liquid, and electrostatic interactions between the nanoparticles and bacteria. These interactions affect the bacterial cell membrane's function, synthesizing of toxic free radicals that cause oxidative stress in the bacteria [4]. This study aims to synthesize and characterize SnO<sub>2</sub> NPs using non-thermal plasma, which is a fast, simple, and cost-effective technique to test SnO<sub>2</sub> NPs' antibacterial capabilities against *Staphylococcus aureus* and *E. coli*.

## 2. Experimental part

### 2.1 Plasma generation mechanism and synthesis of tin oxide nanoparticles

The current investigation synthesized tin oxide nanoparticles using a non-thermal plasma system over water. Water was the liquid used in this study due to its large heat capacity, which functioned as an electrode and maintained the plasma at a relatively low temperature.

The cathodic plasma design that was used in our study involves placing the cathode above the water surface and the anode immersed in the water. SnO<sub>2</sub> NPs were synthesized by argon gas. The thermal conductivity of the inert gas argon is relatively low, which reduces the possibility of the electrode overheating and reduces its oxidation.

Applying an electrical voltage between the electrodes creates a stable discharge plasma at atmospheric pressure between the cathode and the water surface (the anode). This causes the gas to breakdown at the interface. The interface region is of great importance because it is the area of interactions where nanoparticles are synthesized. The cathode emits energetic electrons in the interface region, which can excite and ionize particles in this area. A significant number of secondary electrons and positive ions are generated in the interface region. When water was used as an anode, the interface voltage remained constant, and secondary electrons were transferred from the plasma to the water. Water dissolved the secondary electrons, transforming them into

hydrated electrons ( $e_{aq}^-$ ). The positive hydrogen ions that result from the collision of electrons with water molecules move toward the cathode. Hydrogen ions bombard the cathode's negative surface, transferring kinetic energy to it. This causes momentum transfer and corrosion of the tin anode [5].

In the cathodic plasma design, Fig. 1 shows the synthesis of tin oxide nanoparticles on the water surface after 3 minutes. Moreover, the plasma generation triggered oxidation and reduction reactions by introducing highly reactive species into the water. When plasma interacts with the water surface, it creates highly reactive free radicals like hydrogen radicals (strong reductants), hydroxyl radicals (strong oxidants), or steam. These radicals, which are made up of ions, free electrons or electronically stimulated atoms, separate the water molecules and provide the oxygen needed for the tin to oxidation.

### 2.2 Plasma jet setup to synthesis of SnO<sub>2</sub> NPs

Figure 1 shows the non-thermal plasma jet device used in nanoparticle synthesis. It was placed 1 cm above deionized water containing a tin sheet purchased from Sigma-Aldrich in the USA (1 cm wide, 5 cm long) as an anode that was immersed in a liquid and sprayed with plasma through a stainless-steel needle serving as a cathode (inner circumference 2.5 mm, length 5 cm) at a distance of 3 cm from the anode by using a DC power source and a strong voltage of 13 kV at different times (3 and 5 minutes) to produce tin oxide nanoparticles. Argon was used as the drain gas and connected to the syringe through a glass flowmeter at a rate of 1, 2, and 3 L/min during diagnosis. On the other hand, the flowmeter was set at a 2 L/min rate to synthesize NPs, and as the preparation time progressed, the solution color remained clear with a little change to turbid. Consequently, this serves as an initial indicator of SnO<sub>2</sub> NPs synthesis. The spectral emissions of the generated plasma were determined using a S3000-UV-NIR spectrometer device (Hangzhou Seeman Technology), which has wavelengths ranging be-

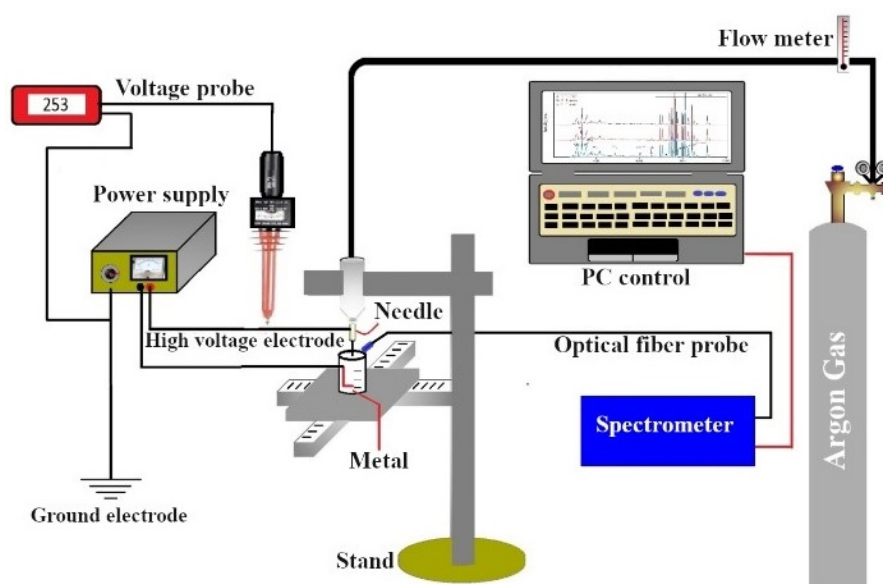


Figure 1. The experimental system.

tween (190–1070 nm) and the spectral resolution is 1.8 nm. The spectrometer was connected to an optical fiber cable (SMA-905) to record spectral emissions and diagnose the operating parameters of argon plasma. The spectral lines were identified using the atomic spectra database (NIST). The electron temperature is the most important parameter that directly describes the average electron kinetic energy in a plasma. The most common method for calculating it is the two ratio method, as shown in the formula below [6].

$$T_e = \left| \frac{\Delta E}{k \ln \left( \frac{I_{mr}/A_{mr}g_m\lambda_{mr}}{I_{nr}/A_{nr}g_n\lambda_{nr}} \right)} \right| \quad (1)$$

$\Delta E = E(m) - E(n)$ , where  $E(m)$  and  $E(n)$  represent the energies of the  $m$  and  $n$  energy levels, respectively,  $k$  is Boltzmann's constant,  $I_{mr}$  and  $I_{nr}$  represent the intensities of related spectral lines, which are the radiation frequencies of electrons that spontaneously transition from the  $m$  and  $n$  energy levels to the  $r$  energy levels,  $A_{mr}$  and  $A_{nr}$  are the transition probabilities,  $\lambda_{mr}$  and  $\lambda_{nr}$  are the corresponding emission spectra's wavelengths, and finally, the statistical weights of particles at the corresponding energy levels are represented by  $g_m$  and  $g_n$ . To measure the electron temperature, we can select two sample  $ArI$  spectral lines (751.46 and 763.51 nm) from the plasma jet's spectra.

The density of electrons plays an important role in diagnosing plasma properties. The measured spectral lines show a significantly broadened line width compared to the natural line width. Plasma broadening occurs through three main processes: moving atoms (Doppler broadening), charged species collisions (Stark broadening), and neutral species collisions on strong resonance lines (resonance broadening) [7]. Stark broadening, which happens when collisions, mostly with plasma electrons, disturb the oxygen atoms' excited states, is the broadening's primary cause. In this case, the effects of Doppler broadening and resonance broadening are not significant. Therefore, these two broadenings are neglected. There is a direct relationship in the quasi-static approximation between the density of the plasma and the FWHM of the Stark broadening line width ( $\Delta\lambda_{OI}$ ) [8].

$$\Delta\lambda_{OI} = 2\omega_{OI}^{exp} \left( \frac{N_e}{10^{16}} \right) \quad (2)$$

where  $N_e$  is the plasma density,  $\omega$  is the electron impact parameter. The correction for Stark broadening in non-hydrogenic ions is expressed as

$$\Delta\lambda_{ion} = 3.5A \left( \frac{N_e}{10^{16}} \right)^{\frac{5}{4}} \left( 1 - \frac{3}{4}N_D^{-\frac{1}{3}} \right) \omega_{OI}^{exp} \quad (3)$$

Here,  $A$  represents the static ion broadening parameter, and  $N_D$  stands for the particle number in the Debye sphere, which is expressed as

$$N_D = 1.72 \times 10^9 T^{\frac{3}{2}} N_e^{-\frac{1}{2}} \quad (4)$$

By adding  $\omega_{OI}^{exp} = 0.0166$  nm,  $A = 0.035$  [8], according to the parameters of plasma obtained in this study ( $N_e \sim 10^{16}$  cm<sup>-3</sup> and  $T \sim 5800$  K), the ions' broadening was 0.01 nm; it was ignored. The plasma frequency is composed of

electron  $\omega_{pe}$  and ion  $\omega_{pi}$  frequencies. The electron plasma frequency is the most important because of the high mobility of electrons. Ions have a lower collision frequency because of their slower thermal velocity than electrons. Therefore, ions collide with other ions less frequently than electrons due to this same factor. Consequently, we can write the plasma frequency of an electron ( $\omega_{pe}$ ) as  $\omega_{pe}$  (Hz) =  $8.98 \sqrt{N_e}$ .

### 2.3 Antibacterial activity assay

The study used the agar-well diffusion method and the standard broth dilution method (CLSI M07-A8) to test how well SnO<sub>2</sub> NPs inhibit the growth of *Escherichia coli* and *Staphylococcus aureus*. Each petri dish was filled with 25 mL of Mueller-Hinton agar in the well diffusion assay. 50  $\mu$ L of both types of bacteria were cultured in Mueller-Hinton broth (MHB) medium for one night at 37 °C. Three wells were created on the agar with appropriate spacing between each well and injected with NPs solution at concentrations of 30, 60, and 90  $\mu$ g/mL. The plates were incubated at 37 °C for 18 to 24 hours. The zones of inhibition (ZOI) were measured after incubation. Agar-well diffusion is a common antibacterial test that assesses a substance's activity against bacteria, with the inhibition zone's diameter influenced by the material's solubility and infusibility. Meanwhile, the minimum inhibitory concentration (MIC) method, which uses tubes of diluted concentrations to detect the minimum concentration inhibiting bacteria growth, can demonstrate more efficacy than the agar-well diffusion method. On the other hand, the minimum inhibitory concentration (MIC) method works better than the agar-well diffusion method. It uses tubes of diluted concentrations to find the lowest concentration that inhibits bacteria from growing. We used seven tubes for each type of bacteria and added 5 mL of MHB to each one. The tube on the right was used as a negative control and only contained MHB. On the other hand, the tube on the left side held MHB mixed with bacteria, serving as a positive control. After that, nanoparticles were added to each of the seven tubes at concentrations of 0.5, 2, 4, 8, 16, 32, and 64  $\mu$ g/mL from a stock solution of 90  $\mu$ g/mL SnO<sub>2</sub> NPs. Following this, 500  $\mu$ L of each type of bacteria that had been prepared was added, with a McFarland concentration of 0.5. The tubes were incubated at 37 °C for 18 to 24 hours. To confirm the MIC for the tested bacteria. The study evaluated the optical turbidity of six groups of tubes before and after incubation.

## 3. Results and discussion

### 3.1 Emission spectra of the non-thermal plasma jet

Figure 2 shows that the argon plasma emission spectra were mostly focused after 690 nm, specifically between 690 and 950 nm, as previously reported in the literature [9]. Several excited argon atomic lines are detected at (696.54, 706.87, 727.29, 738.39, 751.46, 763.51, 772.42, 794.82, 801.48, 811.53, 826.45, 842.46, 852.14, 866.79, 912.30, 922.45, and 965.78 nm). Increasing the argon flow rate directly increases the intensity of these atomic lines. At the same time, several oxygen atomic lines are associated with OI, represented by wavelengths of 715.67, 777.54, and 822.18

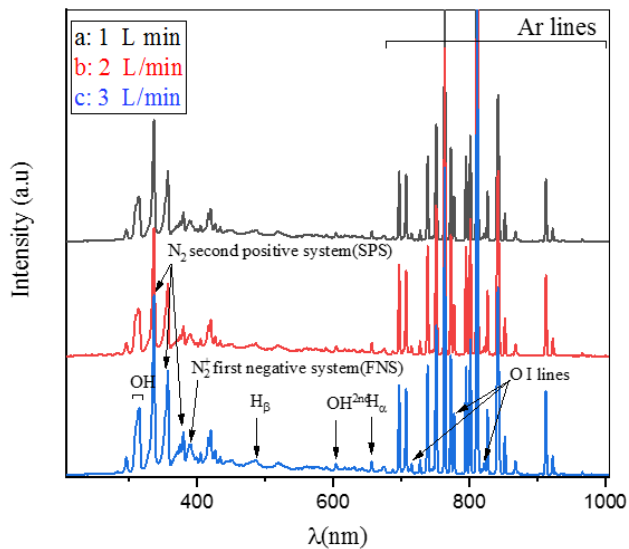


**Figure 2.** Plasma emission spectra at varying flow rates of argon gas, 1 to 3 L/min.

nm. The results are consistent with those reported in references [10, 11]. The plasma is formed in the atmosphere, with a portion of the surrounding air being drawn into the plasma jet. This results in the presence of various active particles that include nitrogen and oxygen. The emission bands and lines of molecular nitrogen have wavelengths ranging from 320 nm to 380 nm. Moreover, the emission lines of hydrogen ( $H_\alpha$ ) are at 656.3 nm and ( $H_\beta$ ) is at 486.13 nm, consistent with the previous study [12]. The emission bands of  $OH^\cdot$  hydroxyl radical at 306 nm to 312 nm, which result from water molecules' dissociation, are present. The results are consistent with several previous studies [9, 13]. In addition to that, the measurement of  $OH^{2nd}$  at 603.45 nm aligns with [12, 14]. The emission spectra of plasma-activated water show reactive nitrogen, such as the  $N_2$  second positive system (SPS) at 335, 356, and 380 nm and the  $N_2^+$  first negative system (FNS) at 391 nm. This suggests that discharge above the water surface may create reactive nitrogen and oxygen species. The energetic electrons collide with oxygen and nitrogen molecules in the surrounding air to form these species [15, 16]. Table 1 shows a direct correlation between the gas flow rate and each of the plasma parameters.

### 3.2 Characterization of $SnO_2$ NPs

Figure 3 shows the crystal structure analysis of the prepared nano-tin oxide samples using an XRD pattern. The obtained

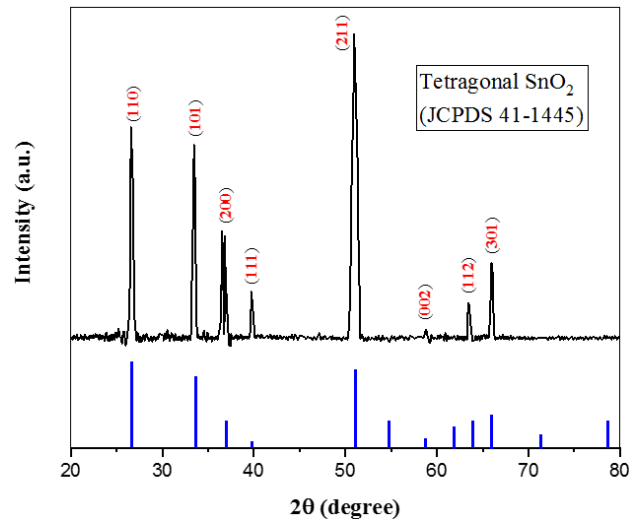


**Figure 3.** XRD pattern of the prepared sample.

sharp diffraction peaks with high crystallinity correspond to the tetragonal rutile structures of  $SnO_2$  (JCPDS, 41-1445). Pure-phase  $SnO_2$  has been successfully formed, as no additional peaks or crystallographic phases have been observed in the sample. The positions of diffraction peaks ( $2\theta$ ) at values of 26.6°, 33.6°, 37.6°, 39.2°, 51.5°, 58°, 64.5°, and 65.9° are corresponding to the (110), (101), (200), (111), (211), (002), (112), and (301) planes, respectively. The well-crystallized  $SnO_2$  NPs can be observed by the sharp and strong diffraction peaks [17]. A comparison of the relative intensities of diffraction peaks in our study showed that (211) is the preferred growth direction of the nanoparticles. Although the structure of  $SnO_2$  in a tetragonal rutile is characterized by (110) being the most thermodynamically stable surface, the other surfaces exhibit slightly less stability. It is possible that the surface relaxation process can lead to ionic displacements and lower the surface energy. As a result, the bonds between surface ions that don't coordinate well with those below them tighten. The synthesis method of NPs plays an important role in these possibilities [18]. The results are in line with the studies [19, 20]. Scherrer formula [21] indicates that  $SnO_2$  has an average crystallite size of 12.45 nm at a preparation time of 3 minutes.

Figure 4 shows FE-SEM images of nanoparticles formed after the tin sheet was exposed to non-thermal plasma for 3 and 5 minutes and then deposited on glass using the drop-cast method. The images show the successful growth of  $SnO_2$  NPs. The non-thermal plasma exposure period is im-

**Table 1.** Plasma parameter data for different flow rates.

Gas flow (L/min)	$T_e$ (eV)	HMFV	$N_e \times 10^{17}$ ( $cm^{-3}$ )	$\omega_{pe} \times 10^{12}$ (Hz)	$\lambda_D \times 10^{-5}$ (cm)	$N_D$ ( $cm^3$ )
1	0.248	2.2225	6.69	7.344	0.452	258.648
2	0.255	2.2417	6.75	7.377	0.457	269.724
3	0.261	2.3399	7.05	7.539	0.452	272.566

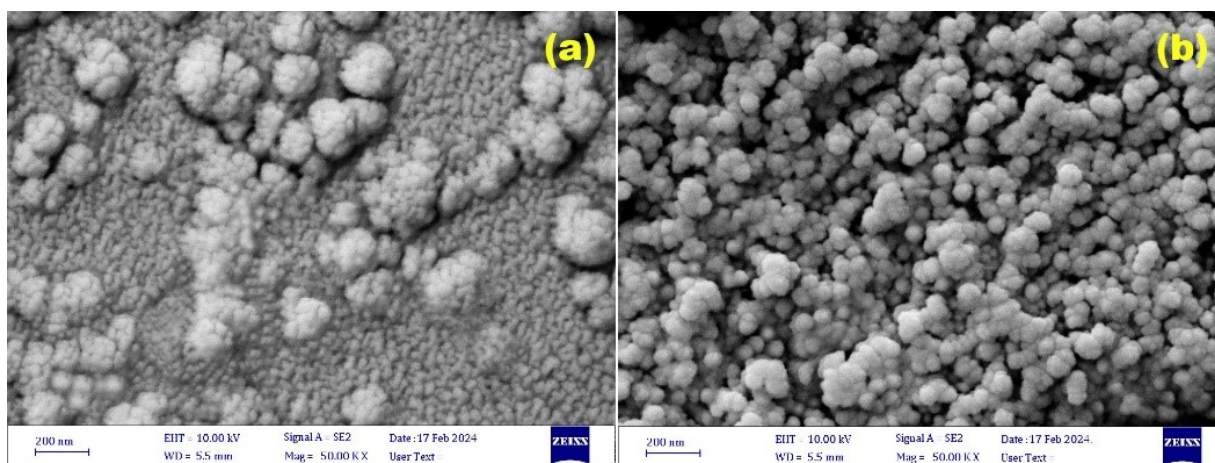


**Figure 4.** FESEM images at magnification 50.00 KX show SnO<sub>2</sub>NPs prepared by the drop-cast method as a function of the preparation time: (a) 3 min; (b) 5 min.

portant to the shape of the formed SnO<sub>2</sub> NPs. According to different exposure times of non-thermal plasma, spherical and homogenous nanoparticles were obtained. The average nanostructure diameters, approximately 25 nm in 3 minutes, increased as the plasma exposure duration reached 45 nm in 5 minutes. Results have shown that the increased period of plasma jet exposure enhances grain growth by allowing smaller grains to merge to form larger ones. The increased surface areas and surface energies are responsible for this. The higher surface area to volume ratio resulted in the merging or aggregation of NPs due to the attractive physical forces between them [22].

Therefore, changing the plasma exposure time can alter the particle aggregation phenomenon. Optimizing the nanoparticles' shape and other characteristics will enhance their inhibitory impact or interaction with pathogenic bacteria. This behavior aligns with studies [23, 24].

UV-vis spectroscopy is a necessary technique for analyzing colloidal liquids. Fig. 5 shows the absorption spectra of synthesized nanoparticles at the wavelength range of 200 – 800 nm. The collective oscillation of free electrons,

or surface plasmon resonance (SPR), affects nanomaterial properties. The height and width of SPR peaks are dependent on the size, shape, and surrounding media. In the UV region, SPR shows absorbance in the peak range (255 – 260 nm); previous literature has confirmed the formation of SnO<sub>2</sub> NPs within this specific range [25, 26]. The solution color shows a clear transition from a clear solution to a turbid white solution with an increase in the plasma's prepared time. There is a clear decrease in absorption spectra, which refers to the transparency of tin oxide to visible light [27]. The bathochromic shift in SPR signal from 255 nm to 260 nm was recorded at an increased preparation time of 3 to 5 minutes, indicating increased SnO<sub>2</sub> particle sizes; this behavior is usually associated with possible aggregating. Furthermore, the strong peaks indicate the synthesized nanoparticles' low crystalline size, high purity, and perfect crystallinity, as reported in the literature [21, 28].

The direct band gap of both SnO<sub>2</sub> samples is calculated from the  $(\alpha h\nu)^2$  versus photon energy ( $h\nu$ ) plot as shown in Fig. 6. The band gap was found to be 3.18 eV and 3.07 eV for the synthesized samples with a preparation time of

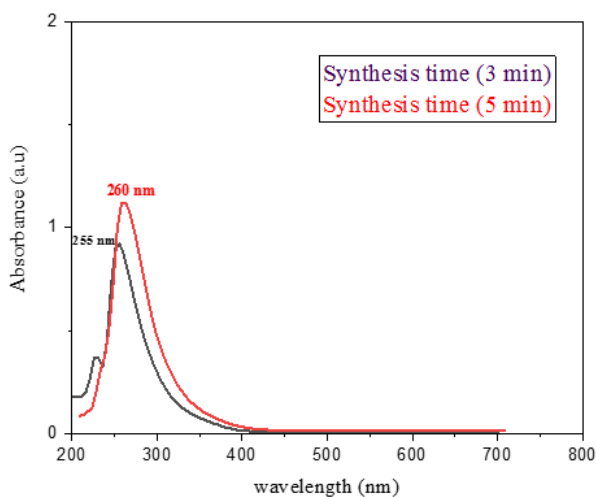


**Figure 5.** The absorption spectra of the synthesized samples.

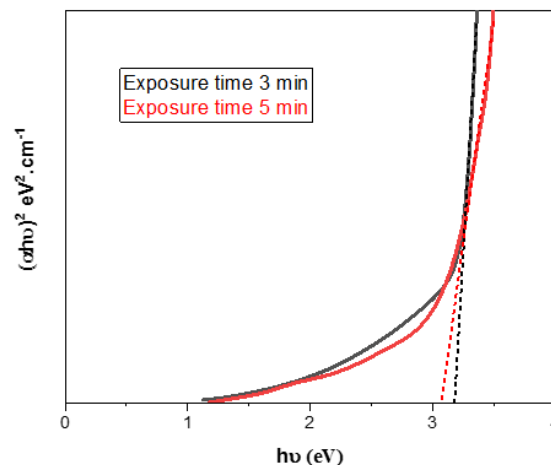


**Figure 6.** Tauc Plot for the energy band gap of the synthesized samples.

plasma (3 and 5 min), respectively. The little decrease in band gap with an increase in plasma exposure time can be attributed to increased crystallinity [29]. Many techniques reported similar results [30].

Zeta potential (ZP) measurements were done using (Zeta-sizer Lab Blue Label, Malvern Instruments Limited, USA). Measurements were taken using two different exposure times of non-thermal plasma (3 and 5 minutes). ZP measurements may be used to evaluate the stability of colloidal particles in solution. The Z-potential of sample (a) was measured to be  $-11.2$  mV at a synthesis time of 3 minutes and  $-5.95$  mV for sample (b) at a synthesis time of 5 minutes (see Fig. 7). Generally, zeta values of ( $\pm 0 - 10$  mV) highly unstable, ( $\pm 10 - 20$  mV) relatively stable, ( $\pm 20 - 30$  mV) moderately stable, and finally values more than ( $\pm 30$  mV) highly stable, as reported in the literature [31]. Consequently, this outcome suggests that the particles are relatively stable colloids and can aggregate if left for a long time before solidifying into films on glass substrates or other surfaces, aligning with visual observations.

The present study used inductively coupled plasma mass spectrometry, or ICP-MS technology, to estimate the concentration of the synthesized nanoparticles in solution or liquid. The study found that the non-thermal plasma completely ablates or synthesizes the nanoparticles from the metal tin sheet. The concentration of Sn NPs was  $90 \mu\text{g/mL}$  at three minutes and  $100 \mu\text{g/mL}$  at five minutes. However, determining whether impurities, like oxygen, bound to the tin to form  $\text{SnO}_2$  or if the tin metal Sn was free in solution proved challenging. This is due to the inability of ICP-MS technology to distinguish whether the metal is free or bound. Finally, the study found a direct correlation between plasma exposure duration and increased tin concentration in the solution.

### 3.3 Antibacterial activity

Figure 8 shows that  $\text{SnO}_2$  NPs effectively inhibited both types of bacteria at a concentration of  $90 \mu\text{g/mL}$  compared to other concentrations. The size and shape of  $\text{SnO}_2$  NPs significantly impact their ability to inhibit bacteria. The smaller NPs increase their antibacterial activity when they

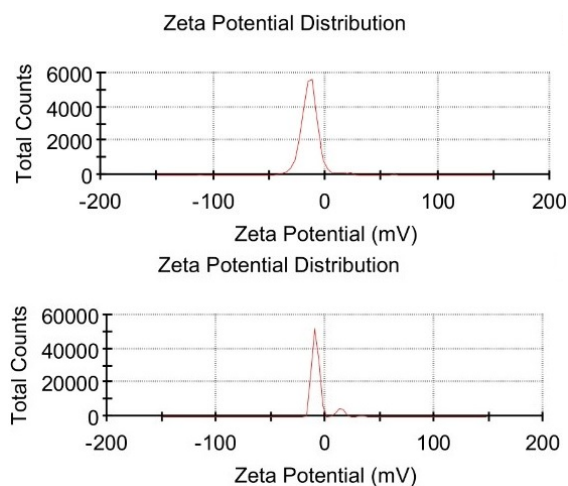


**Figure 7.** ZP results of the synthesized samples.

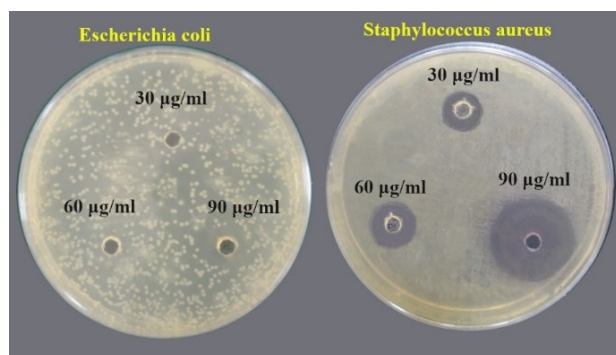


**Figure 8.** Images showing the antibacterial activity of  $\text{SnO}_2$  NPs on two types of bacteria.

aggregate with bacterial effluent, as they expose more of their surface to the bacterial membrane. Having such a large contact surface will significantly improve microbe elimination. As a result, the nanoparticles bind to the bacteria's cell wall and dilapidate the membrane's permeability, causing cell death. However, achieving a small size is not the sole objective. The formulation of bactericidal materials is particularly concerned with synthesizing and characterizing nanoscale materials and their characteristics [32]. The study found that  $\text{SnO}_2$  NPs had a higher inhibitory influence on the gram-positive bacteria than the gram-negative bacteria, as shown by the inhibition values in Table 2. This could be due to variations in the chemical structure and composition of the bacteria's cell wall. The cell walls of Gram-positive bacteria are thicker than those of Gram-negative bacteria. Gram-positive bacteria have a thick, porous peptidoglycan layer in their cell wall. This makes it easier for antibacterial agents to penetrate inside and/or interact with the peptidoglycan itself, causing cell death. This is in addition to their varying sensitivity to metal oxide nanoparticles. The charge on the outer wall of the Gram-positive bacterial cell is greater than that of the Gram-negative, which enhances their ability to attract nanoparticles. Nanoparticles' small size at lower temperatures allows them to penetrate and dilapidate the cell wall, causing cell death [33].

The standard broth dilution method (CLSI M07-A8) is used in determining the minimum inhibitory concentration (MIC) of nanoparticles that visually inhibit microorganism growth by 99% [34]. Fig. 9 showed that  $\text{SnO}_2$  NPs effectively inhibited the growth of both types of bacteria, but there were variations due to the differences in cell walls and sensitivity

**Table 2.** Values ZOI as a result of  $\text{SnO}_2$  NPs' action against the bacteria *E. coli* and *Staphylococcus aureus*.

Concentration of $\text{SnO}_2$ NPs ( $\mu\text{g/mL}$ )	<i>E. coli</i>	<i>Staphylococcus aureus</i>
30	0	15.344
60	0	17.465
90	17.202	30.665

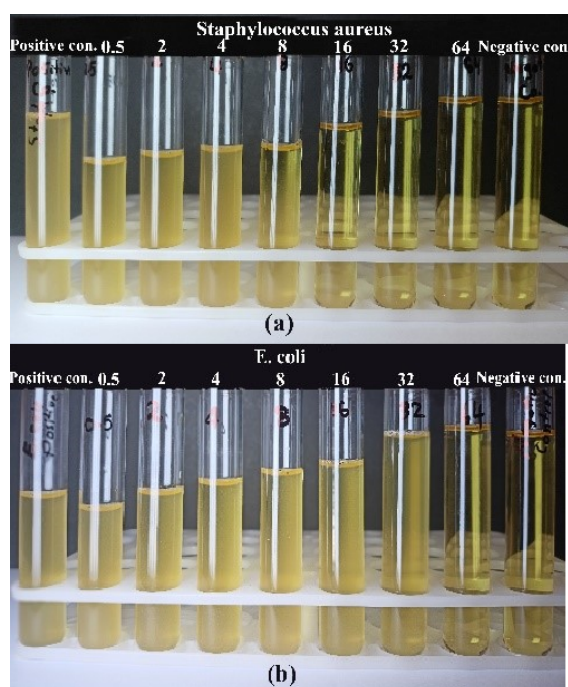


**Figure 9.** Experimental antibacterial activity test tubes of SnO<sub>2</sub> NPs by the MIC method.

to metal oxide nanoparticles. Nanoparticles can destroy microorganisms by causing intracellular material leakage through hole formation on cell walls, which is caused by the oxidation of cell liposaccharides [35]. The MIC results for SnO<sub>2</sub> NPs at different concentrations against *Staphylococcus aureus* significantly inhibited bacterial growth. After incubation, three tubes (16, 32, and 64 mg/mL) showed no bacterial growth after incubation. The optimal MIC for *E. coli* bacteria was only 64 µg/mL. These results confirm that Gram-positive bacteria respond more to SnO<sub>2</sub> NPs compared to Gram-negative bacteria.

#### 4. Conclusion

In conclusion, the non-thermal plasma jet technique is a rapid, simple, low-cost, and scalable technology that can synthesize a SnO<sub>2</sub> NPs solution. The UV-vis analysis shows a transition in color from a clear solution to a turbid white solution during the applied plasma; the results confirm the production of a colloidal solution containing SnO<sub>2</sub> NPs. The SPR peak at around 255–260 nm also confirms the synthesis of highly crystalline SnO<sub>2</sub> NPs. The XRD test shows the creation of pure-phase SnO<sub>2</sub>, which is shown as tetragonal rutile structures (JCPDS, 41–1445). The morphology analysis by FE-SEM shows that particles are spherical and homogenous nanoparticles whose size and distribution depend on the preparation time. ZP indicates that SnO<sub>2</sub> NPs colloids have acceptable stability. The antibacterial activity of SnO<sub>2</sub> NPs was studied using the agar-well diffusion method. As a result, the nanoparticles can inhibit both types of bacteria (*E. coli* and *Staphylococcus aureus*), so they can be used as an antibacterial agent. The MIC results from this study also show that SnO<sub>2</sub> NPs have an effective antibacterial

concentration of 16 µg/mL against *Staphylococcus aureus* bacteria and 64 µg/mL against *E. coli*.

#### Authors contributions

Omar O. Abdulhadi: data curation, formal analysis, investigation, writing-original draft and writing-review & editing. A. S. Obaid: supervision, investigation, project administration, and writing-review & editing. Hamsa A. Ali: formal analysis, methodology and writing-review & editing.

#### Availability of data and materials

The data that support the findings of this study are available from the corresponding author upon reasonable request.

#### Conflict of interests

The author declare that they have no known competing financial interests or personal relationships that could have appeared to influence the work reported in this paper.

#### Open access

This article is licensed under a Creative Commons Attribution 4.0 International License, which permits use, sharing, adaptation, distribution and reproduction in any medium or format, as long as you give appropriate credit to the original author(s) and the source, provide a link to the Creative Commons license, and indicate if changes were made. The images or other third party material in this article are included in the article's Creative Commons license, unless indicated otherwise in a credit line to the material. If material is not included in the article's Creative Commons license and your intended use is not permitted by statutory regulation or exceeds the permitted use, you will need to obtain permission directly from the OICC Press publisher. To view a copy of this license, visit <https://creativecommons.org/licenses/by/4.0>.

#### References

- [1] M. Kolář, K. Urbánek, and T. Látal. “Antibiotic selective pressure and development of bacterial resistance.”. *Int J Antimicrob Agents*, **17**:357–363, 2001. DOI: [https://doi.org/10.1016/S0924-8579\(01\)00317-X](https://doi.org/10.1016/S0924-8579(01)00317-X).
- [2] M. Fernández-García, A. Martínez-Arias, J. C. Hanson, and J. A. Rodriguez. “Nanostructured oxides in chemistry: Characterization and properties.”. *Chem Rev*, **104**:4063–4104, 2004. DOI: <https://doi.org/10.1021/cr030032f>.
- [3] F. Rezaei, P. Vanraes, A. Nikiforov, R. Morent, and N. De Geyter. “Applications of plasma-liquid systems: a review.”. *Materials*, **12**:2751, 2019. DOI: <https://doi.org/10.3390/ma12172751>.

- [4] N. John, M. Somaraj, and N. J. Tharayil. "Synthesis, characterization and anti-bacterial activities of SnO<sub>2</sub> nanoparticles using biological molecule. ". *IOP Conf Ser Mater Sci Eng*, **360**:012007, 2018. DOI: <https://doi.org/10.1088/1757-899X/360/1/012007>.
- [5] F. Baharlounezhad, M. A. Mohammadi, and M. S. Zakerhamidi. "Plasma-based one-step synthesis of tungsten oxide nanoparticles in short time. ". *Sci Rep*, **13**:7427, 2023. DOI: <https://doi.org/10.1038/s41598-023-34612-y>.
- [6] G. C. Chen, L. M. He, B. B. Zhao, H. L. Zhang, Z. C. Zhao, H. Zeng, J. P. Lei, and X. Liu. "Effects of working medium gases on emission spectral and temperature characteristics of a plasma igniter. ". *Journal of Spectroscopy*, **2019**:1–10, 2019. DOI: <https://doi.org/10.1155/2019/5395914>.
- [7] M. A. Hafez, M. A. Khedr, F. F. Elaksher, and Y. E. Gamal. "Characteristics of Cu plasma produced by a laser interaction with a solid target. ". *Plasma Sources Sci Technol*, **12**:185–198, 2003. DOI: <https://doi.org/10.1088/0963-0252/12/2/310>.
- [8] J. Bernhardt, W. Liu, F. Théberge, H. L. Xu, J. F. Daigle, M. Châteauneuf, J. Dubois, and S. L. Chin. "Spectroscopic analysis of femtosecond laser plasma filament in air. ". *Opt Commun*, **281**:1268–1274, 2008. DOI: <https://doi.org/10.1016/j.optcom.2007.10.100>.
- [9] W. Jiang, J. Tang, Y. Wang, W. Zhao, and Y. Duan. "Characterization of argon direct-current glow discharge with a longitudinal electric field applied at ambient air. ". *Sci Rep*, **34**:1–10, 2014. DOI: <https://doi.org/10.1038/srep06323>.
- [10] F. Rezaei, A. Nikiforov, R. Morent, and N. De Geyter. "Plasma modification of poly lactic acid solutions to generate high quality electrospun PLA nanofibers. ". *Sci Rep*, **8**:2241, 2018. DOI: <https://doi.org/10.1038/s41598-018-20714-5>.
- [11] A. Sarani, A. Y. Nikiforov, and C. Leys. "Atmospheric pressure plasma jet in Ar and Ar/H<sub>2</sub>O mixtures: Optical emission spectroscopy and temperature measurements. ". *Phys Plasmas*, **17**:635041–635048, 2010. DOI: <https://doi.org/10.1063/1.3439685>.
- [12] R. R. Khanikar, H. Bailung, R. R. Khanikar, and H. Bailung. "Cold atmospheric pressure plasma technology for biomedical application. ". *Plasma Sci. Technol*, , 2021. DOI: <https://doi.org/10.3390/mi11030242>.
- [13] H. Pan, G. Wang, J. Pan, G. Ye, K. Sun, J. Zhang, and J. Wang. "Cold plasma-induced surface modification of heat-polymerized acrylic resin and prevention of early adherence of *Candida albicans*. ". *Dental materials journal*, **34**:529–536, 2015. DOI: <https://doi.org/10.4012/dmj.2015-035>.
- [14] P. Bruggeman and C. Leys. "Non-thermal plasmas in and in contact with liquids. ". *J Phys D Appl Phys*, **42**:053001, 2009. DOI: <https://doi.org/10.1088/0022-3727/42/5/053001>.
- [15] Y. J. Hong, C. J. Nam, K. B. Song, G. S. Cho, H. S. Uhm, D. I. Choi, and E. H. Choi. "Measurement of hydroxyl radical density generated from the atmospheric pressure bioplasma jet. ". *Journal of Instrumentation*, **7**:C03046, 2012. DOI: <https://doi.org/10.1088/1748-0221/7/03/C03046>.
- [16] L. Potočnáková, J. Hnilica, and V. Kudrle. "Spatially resolved spectroscopy of an atmospheric pressure microwave plasma jet used for surface treatment. ". *Open Chem*, **13**:541–548, 2015. DOI: <https://doi.org/10.1515/chem-2015-0066>.
- [17] R. Mani, K. Vivekanandan, and A. Jegatheesan. "High performance photocatalytic activity of pure and Ni doped SnO<sub>2</sub> nanoparticles by a facile wet chemical route. ". *Journal of Materials Science: Materials in Electronics*, **29**:6308–6315, 2018. DOI: <https://doi.org/10.1007/s10854-018-8610-6>.
- [18] J. Oviedo and M. J. Gillan. "Energetics and structure of stoichiometric SnO<sub>2</sub> surfaces studied by first-principles calculations. ". *Surf Sci*, **463**:93–101, 2000. DOI: [https://doi.org/10.1016/S0039-6028\(00\)00612-9](https://doi.org/10.1016/S0039-6028(00)00612-9).
- [19] D. Narsimulu, N. Naresh, B. N. Rao, and N. Satyanarayana. "Rational design of SnO<sub>2</sub> nanoflakes as a stable and high rate anode for lithium-ion batteries. ". *Journal of Materials Science: Materials in Electronics*, **31**:8556–8563, 2020. DOI: <https://doi.org/10.1007/s10854-020-03391-x>.
- [20] S. Kumar, Bhawna, S. K. Yadav, A. Gupta, R. Kumar, J. Ahmed, M. Chaudhary, Suhas, and V. Kumar. "B-doped SnO<sub>2</sub> nanoparticles: a new insight into the photocatalytic hydrogen generation by water splitting and degradation of dyes. ". *Environmental Science and Pollution Research*, **29**:47448–47461, 2022. DOI: <https://doi.org/10.1007/s11356-022-18946-0>.
- [21] O. O. Abdulhadi, I. A. Rahmman, and A. S. Obaid. "Characterizing of chromium oxide nanoparticles formation from solution plasma synthesis by plasma jet. ". *4th International Conference on Materials Engineering & Science AIP Conf.*, :20121–20129, 2022. DOI: <https://doi.org/10.1063/5.0126414>.
- [22] R. S. Mohammed, K. A. Aadim, and K. A. Ahmed. "Synthesis of CuO/ZnO and MgO/ZnO Core/Shell nanoparticles with plasma jets and study of their structural and optical properties. ". *Karbala International Journal of Modern Science*, **8**:88–97, 2022. DOI: <https://doi.org/10.33640/2405-609X.3225>.
- [23] I. K. Abbas and K. A. Adim. "Synthesis and characterization of magnesium oxide nanoparticles by atmospheric non-thermal plasma jet. ". *Kuwait Journal of Science*, **50**:223–230, 2023. DOI: <https://doi.org/10.1016/j.kjs.2023.05.008>.

- [24] M. Li, X. Wang, H. Li, H. Di, X. Wu, C. Fang, and B. Yang. "Preparation of photoluminescent single crystalline MgO nanobelts by DC arc plasma jet CVD." *Appl Surf Sci*, **274**:188–194, 2013. DOI: <https://doi.org/10.1016/j.apsusc.2013.03.013>.
- [25] B. A. Thoker, A. A. Bhat, A. K. Wani, M. A. Kaloo, and G. A. Shergojri. "Preparation and characterization of SnO<sub>2</sub> nanoparticles for antibacterial properties." *Nanomaterial Chemistry and Technology*, **2**:1–5, 2020. DOI: <https://doi.org/10.33805/2690-2575.109>.
- [26] N. M. Al-Enazi, F. Ameen, K. Alsamhary, T. Dawoud, F. Al-Khattaf, and S. AlNadhari. "Tin oxide nanoparticles (SnO<sub>2</sub>-NPs) synthesis using *Galaxaura elongata* and its anti-microbial and cytotoxicity study: a greenery approach." *Appl Nanosci*, **13**:519–527, 2023. DOI: <https://doi.org/10.1007/s13204-021-01828-1>.
- [27] V. S. Jahnvi, S. K. Tripathy, and A. V. N. Ramalingeswara Rao. "Structural, optical, magnetic and dielectric studies of SnO<sub>2</sub> nanoparticles in real time applications." *Physica B Condens Matter*, **565**:61–72, 2019. DOI: <https://doi.org/10.1016/j.physb.2019.04.020>.
- [28] O. O. Abdulhadi, I. A. Rahmman, and A. S. Obaid. "Synthesis and characterization of nickel nanoparticles formed by solution cold plasma jet." *Journal of Physics: Conference Series (IOP)*, :1–12, 2021. DOI: <https://doi.org/10.1088/1742-6596/2114/1/012083>.
- [29] Y. Kuang, V. Zardetto, R. van Gils, S. Karwal, D. Koushik, M. A. Verheijen, L. E. Black, C. Weijtens, et al. "Low-temperature plasma-assisted atomic-layer-deposited SnO<sub>2</sub> as an electron transport layer in planar perovskite solar cells." *ACS Appl Mater Interfaces*, **10**:30367–30378, 2018. DOI: <https://doi.org/10.1021/acsami.8b09515>.
- [30] Md. T. Rahman, Z. Ahmed, Md. J. Islam, K. Jobayer, Mst. A. Amuda Khatun, Md. A. Gafur, M. S. Bashar, and M. Monjarul Alam. "Comparative study of structural, optical and electrical properties of SnO<sub>2</sub> thin film growth via CBD, drop-cast and dip-coating methods." *Materials Sciences and Applications*, **12**:578–594, 2021. DOI: <https://doi.org/10.4236/msa.2021.1212038>.
- [31] S. Bhattacharjee. "DLS and zeta potential - What they are and what they are not?". *Journal of Controlled Release*, **235**:337–351, 2016. DOI: <https://doi.org/10.1016/j.jconrel.2016.06.017>.
- [32] S. Pal, Y. K. Tak, and J. M. Song. "Does the antibacterial activity of silver nanoparticles depend on the shape of the nanoparticle? A study of the Gram-negative bacterium *Escherichia coli*." *Appl Environ Microbiol*, **73**:1712–1720, 2007. DOI: <https://doi.org/10.1128/AEM.02218-06>.
- [33] S. A. Khan, S. Shahid, S. Hanif, H. S. Almoalim, S. A. Alharbi, and H. Sellami. "Green synthesis of chromium oxide nanoparticles for antibacterial, antioxidant anticancer, and biocompatibility activities." *Int J Mol Sci*, **22**:502, 2021. DOI: <https://doi.org/10.3390/ijms22020502>.
- [34] R. Krishnan, V. Arumugam, and S. K. Vasaviah. "The MIC and MBC of silver nanoparticles against enterococcus faecalis - a facultative anaerobe." *J Nanomed Nanotechnol*, **6**:1–4, 2023. DOI: <https://doi.org/10.4172/2157-7439.1000285>.
- [35] S. Ghasemizad, S. Pirsā, S. Amiri, and P. Abdosattari. "Optimization and characterization of bioactive biocomposite film based on orange peel incorporated with Gum arabic reinforced by Cr<sub>2</sub>O<sub>3</sub> nanoparticles." *J Polym Environ*, **30**:2493–2506, 2022. DOI: <https://doi.org/10.1007/s10924-021-02357-2>.